Available online at www.sciencedirect.com
SCIENCE DIRECT®
Journal of Sound and Vibration 279 (2005) 1131–1154
JOURNAL OF SOUND AND VIBRATION
www.elsevier.com/locate/jsvi

Modelling of fine-scale turbulence mixing noise

A. Khavaran[a,*], J. Bridges[b]

[a] QSS Group, Inc., NASA Glenn Research Center, Cleveland, OH 44135, USA
[b] Acoustics Branch, NASA Glenn Research Center, Cleveland, OH 44135, USA

Received 5 August 2002; accepted 30 November 2003

Abstract

The present paper is a study of aerodynamic noise spectra from model functions that describe the source. The study is motivated by the need to improve the spectral shape of the MGBK jet noise prediction methodology at high frequency.

The predicted spectral shape usually appears less broadband than measurements and faster decaying at high frequency. Theoretical representation of the source is based on Lilley's equation. Numerical simulations of high-speed subsonic jets as well as some recent turbulence measurements reveal a number of interesting statistical properties of turbulence correlation functions that may have a bearing on radiated noise. These studies indicate that an exponential spatial function may be a more appropriate representation of a two-point correlation compared to its Gaussian counterpart. The effect of source non-compactness on spectral shape is discussed. It is shown that source non-compactness could well be the differentiating factor between the Gaussian and exponential model functions.

In particular, the fall-off of the noise spectra at high frequency is studied and it is shown that a non-compact source with an exponential model function results in a broader spectrum and better agreement with data. A recent source model proposed by Tam and Auriault that represents the source as a covariance of the convective derivative of fine-scale turbulence kinetic energy is also examined.

1. Introduction

A physics-based methodology utilizing the averaged equations of motion is used to assess jet noise spectra as a function of the source model function. The focus here is small-scale turbulence noise that dominates the spectra at subsonic Mach numbers. It is generally accepted that sound generation in jets is a by-product of the unsteady features of the flow. Any flow manipulation

*Corresponding author.
E-mail address: khavaran@grc.nasa.gov (A. Khavaran).

0022-460X/$ - see front matter © 2004 Elsevier Ltd. All rights reserved.
doi:10.1016/j.jsv.2003.11.054

intended to reshape the spectra and subsequent perceived noise level ought to affect the unsteady characteristics of the flow.

Mixing enhancement devices such as chevrons and tabs are known to alter turbulence statistics [1] and change the time- and length-scales of noise generating eddies. These flow modifications directly impact the sound field by, for example, reducing the low-frequency noise at the cost of adding to the high-frequency content. As such, it is not unreasonable to argue that modelling of the unsteady behavior of the flow as supported by a number of isolated test configurations may not lead to a reliable prediction tool. In an ideal situation, one might attempt to solve the full compressible Navier Stokes equations without resorting to any modelling closures. In fact, it is simply a matter of time before Direct Numerical Simulations (DNS) should solve the far-field jet acoustics either directly or by some extension of the near-field solution [2]. Clearly, the computational demands of a typical high Reynolds number jet leave little room, at least in the near future, for DNS as a design code. Nevertheless, it could be an extremely useful tool in understanding the unsteady features of the jet in order to improve the source modelling.

On the other hand, the computational requirements are greatly reduced if the governing equations are spatially filtered, as is done in the large eddy simulation (LES) [3–5], and the effect of subgrid scales (SGS) is modelled. This approach is successful in capturing the distinct directivity of supersonic jets that result from large scales of motion (instability waves) that dominate the general noise picture near the down-stream axis. But it might also suffer from a neglect of high-frequency noise resulting from sub-grid scales. A recent study by Seror et al. [6] calculates the acoustic pressure from the filtered Lighthill's stress tensor as well as the full tensor and concludes that the SGS part of the tensor needs to be taken into account in order to recover reliable high-frequency results. One must also be careful about the selection of the subgrid scale model as well as the inflow perturbations used in the simulation [7]. LES predictions of Morris et al. [3] appear to benefit from the dynamic subgrid model and narrow down some of the usual over-predictions in turbulence and noise.

Physics-based prediction methods such as MGBK [8] or Tam and Auriault's fine-scale model [9] heavily rely on model functions that express the statistical properties of noise sources. These predictions use the averaged equations of motion; hence the unsteady features of the flow are entirely described by two-point, space–time correlation models. Any shortcoming in the predictions should be directly linked to the model as well as the accuracy of the RANS predictions. As a post processor, MGBK takes advantage of the latest developments in turbulence modelling in its noise predictions. Presently, the Reynolds-averaged Navier–Stokes (RANS) solution is generated using WIND [10] flow solver provided by the NPARC Alliance. In addition to the source strength, other phenomena such as refraction and convection impact the directivity of jet noise.

Woodruff et al. [11] study the isotropic source model in the original MGBK noise prediction methodology [12] and examine alternative representations for the turbulence spectra. They propose an energy spectrum function for the two-point velocity correlation to satisfy the Kolmogoroff spectrum law [13] in the inertial sub-range. In particular, they examine a wave-number-dependent Gaussian function for the temporal part of the correlation, as opposed to the usual separable space and time functions. Here the characteristic frequency is scaled based on spatial wave-number k and turbulence dissipation rate ε as $\tau_o^{-1} \sim k^{2/3}\varepsilon^{1/3}$. The predicted spectra do

not appear to offer noticeable improvement over the conventional MGBK methodology that uses a separable correlation function and calculates a characteristic frequency from turbulence kinetic energy κ as $\tau_o^{-1} \sim \kappa/\varepsilon$. Nonetheless, near 90° angle, they report slight improvement in their spectral shape.

Tam and Auriault [9] model their source as a two-point correlation of the convective derivative of kinetic energy of small-scale turbulence. They use RANS to calculate the time- and length-scales of the noise sources as is done in the MGBK, and predict noise spectra in good agreement with data at mid angles.

In all, the noise from small scales of motion, which are usually broadband in nature and cover a range of observer angles, remains a significant part of the jet noise spectra. Indications are that at high subsonic Mach numbers, and heated jets in particular, instability-associated noise may dominate the low end of the spectra at shallow angles. On the other hand, one might argue that the mean-flow effects could also play a role, by diverting the high-frequency noise of small-scale turbulence away from the axis, and creating a region near the zone of silence that is dominated by low-frequency noise.

In this work, alternative representations of the source in modeling the quadrupole terms of Lilley's equation are examined. Discussions concentrate on a 90° emission angle where shear-noise is not a factor and the spectral shape is predominantly defined by the self-noise component. The paper begins with some preliminary formulation of the governing equations. Section 2.2 derives expressions for source and non-compactness factor as a function of the proposed models. It is shown that the fall-off of the high-frequency noise becomes less steep when an exponential spatial function with an appropriate temporal function is selected and non-compactness effects are included. Section 3 compares Tam and Auriault's model [9] with the MGBK model as proposed in Ref. [8]. It concludes that the spectral shape at 90° should be identical if consistent assumptions are used. Some concluding remarks on future directions for a physics-based modelling approach is given in Section 4.

2. Sound spectral density

Application of Lilley's equation to the problem of jet noise and the significance of various source terms has been the subject of numerous discussions in aeroacoustics. In a recent article, Goldstein [14] gives an exact form of the equation with the dependent variable defined such that the source is of a quadrupole/dipole nature. The quadrupole source is second-order in velocity fluctuations and is the sum of the commonly known self- and shear noise terms as introduced by Lilley. The dipole term is produced by the fluctuating sound speed due to temperature fluctuations.

The far-field spectral density due to sources of Lilley's equation may be expressed as integration over the source volume $\mathbf{y}$,

$$\overline{p^2}(\mathbf{x}|\omega) = \int_{\mathbf{y}} \int_{\xi} G^*(\mathbf{x}, \mathbf{y} - \xi/2, \omega) G(\mathbf{x}, \mathbf{y} + \xi/2, \omega) Q_{12}(\mathbf{y}, \xi, \omega)\, \mathrm{d}\xi\, \mathrm{d}\mathbf{y}, \tag{1}$$

where G is an appropriate Green's function, * denotes a complex conjugate, and Q_{12} is the source spectral density which is formed from a Fourier transform of a two-point space–time correlations

between source points $\mathbf{y}_1 = \mathbf{y} - \boldsymbol{\xi}/2$ and $\mathbf{y}_2 = \mathbf{y} + \boldsymbol{\xi}/2$ separated by time τ,

$$Q_{12}(\mathbf{y}, \boldsymbol{\xi}, \omega) = \int_{-\infty}^{+\infty} R(\mathbf{y}, \boldsymbol{\xi}, \tau) \mathrm{e}^{\mathrm{i}\omega\tau} \, \mathrm{d}\tau. \tag{2}$$

If the variation of the magnitude of the Green's function with respect to $\boldsymbol{\xi}$, within the source region where Q_{12} is non-zero, is assumed negligible compared to that of its phase then

$$G^*(\mathbf{x}, \mathbf{y} - \boldsymbol{\xi}/2, \omega) G(\mathbf{x}, \mathbf{y} + \boldsymbol{\xi}/2, \omega) \approx |G(\mathbf{x}, \mathbf{y}, \omega)|^2 \mathrm{e}^{-\mathrm{i}\mathbf{k}.\boldsymbol{\xi}}, \tag{3}$$

where $\mathbf{k}$ is a wave number of magnitude (ω/a_∞) and direction $(\mathbf{x} - \mathbf{y})$. Here ω is the frequency at the observer location $\mathbf{x}$ and a_∞ denotes the ambient sound speed. Eq. (1) is now written as

$$\overline{p^2}(\mathbf{x}|\omega) = \int_{\mathbf{y}} |G(\mathbf{x}, \mathbf{y}, \omega)|^2 \int_{-\infty}^{\infty} \mathrm{e}^{\mathrm{i}\omega\tau} \, \mathrm{d}\tau \int_{\boldsymbol{\xi}} R(\mathbf{y}, \boldsymbol{\xi}, \tau) \mathrm{e}^{-\mathrm{i}\mathbf{k}.\boldsymbol{\xi}} \, \mathrm{d}\boldsymbol{\xi} \, \mathrm{d}\mathbf{y}. \tag{4}$$

It is argued that changes in retarded time across a correlation volume element are more likely to be small if the correlation is written in a frame $\mathbf{x}'$ moving with convection velocity U_c of the turbulent eddies (i.e. $\mathbf{x}' = \mathbf{x} - \mathbf{i}U_c t$). Experimentally, the correlation $R(\mathbf{y}, \boldsymbol{\xi}, \tau)$ in a jet flow describes a fluctuating pattern in a moving frame and is expressed as

$$R_m(\mathbf{y}, \boldsymbol{\xi}_m, \tau) = R(\mathbf{y}, \boldsymbol{\xi}, \tau), \quad \boldsymbol{\xi}_m = \boldsymbol{\xi} - \mathbf{i}U_c\tau. \tag{5}$$

The source frequency Ω is related to the observer frequency through the usual Doppler effect $\Omega = \omega(1 - M_c \cos\theta)$. Making a transformation to the moving frame, one finds $-\mathbf{k}.\boldsymbol{\xi} + \omega\tau = -\mathbf{k}.\boldsymbol{\xi}_m + \Omega\tau$, therefore

$$\int_{-\infty}^{+\infty} \mathrm{e}^{\mathrm{i}\omega\tau} \, \mathrm{d}\tau \int_{\boldsymbol{\xi}} R(\mathbf{y}, \boldsymbol{\xi}, \tau) \mathrm{e}^{-\mathrm{i}\mathbf{k}.\boldsymbol{\xi}} \, \mathrm{d}\boldsymbol{\xi} \equiv \int_{-\infty}^{+\infty} \mathrm{e}^{\mathrm{i}\Omega\tau} \, \mathrm{d}\tau \int_{\boldsymbol{\xi}_m} R_m(\mathbf{y}, \boldsymbol{\xi}_m, \tau) \mathrm{e}^{-\mathrm{i}\mathbf{k}.\boldsymbol{\xi}_m} \, \mathrm{d}\boldsymbol{\xi}_m. \tag{6}$$

Now the noise spectral density with respect to the moving frame is given as

$$\overline{p^2}(\mathbf{x}|\omega) = \int_{\mathbf{y}} |G(\mathbf{x}', \mathbf{y}, \Omega)|^2 \int_{-\infty}^{\infty} \mathrm{e}^{\mathrm{i}\Omega\tau} \, \mathrm{d}\tau \int_{\boldsymbol{\xi}_m} R_m(\mathbf{y}, \boldsymbol{\xi}_m, \tau) \mathrm{e}^{-\mathrm{i}\mathbf{k}.\boldsymbol{\xi}_m} \, \mathrm{d}\boldsymbol{\xi}_m \, \mathrm{d}\mathbf{y}. \tag{7}$$

2.1. Self noise spectra

For brevity, the subscript m is suppressed in this section, and $\boldsymbol{\xi}$ is used as the separation vector with respect to a moving frame.

To assess the far-field mean-square pressure due to the self-noise term only, Lilley's equation is written in a co-ordinate $\mathbf{x}'$ moving with convection velocity U_c,

$$L(p_{self}; V, x_1') = D\left(\rho \frac{\partial^2 (u_i u_j)}{\partial x_i' \partial x_j'}\right). \tag{8}$$

Here L is the Lilley operator, $V = U - U_c$, and the density ρ has been moved to the right of operator $D = \partial/\partial t + V\partial/\partial x_1'$ assuming that flow is locally parallel and that density fluctuations are small so ρ is the mean density. The Green's function to the above equation for a source of

type $D\{e^{-i\Omega t}\delta(\mathbf{x}' - \mathbf{x}'_o)\}$ is

$$L(Se^{-i\Omega t}; V, x'_1) = D\{e^{-i\Omega t}\delta(x')\delta(\varphi - \varphi_o)\delta(r - r_o)/r\}. \tag{9}$$

In the high frequency limit, S is given as [15]

$$S(\mathbf{x}', \mathbf{y}, \Omega) = \frac{1}{4\pi R}\frac{a_o/a_\infty}{(1 - M_c\cos\theta)(1 - M_o\cos\theta)}\left(\frac{\zeta_o}{r_o g_o}\right)^{1/2} \times e^{i\Omega R/a_\infty} e^{i\,\Omega/a_\infty\left[\int_0^\infty (g-g_\infty)\,dr - \zeta_o\cos(\varphi-\varphi_o)\right]}, \tag{10}$$

where

$$\zeta = \int_0^r g(r,\theta)\,dr. \tag{11}$$

Subscript o refers to source location and the shielding function $g(r,\theta)$ is defined in Appendix A.

The above expression for S is applicable outside the zone of silence of a source only, where the shielding function $g^2(r,\theta)$ is positive at all radial positions; hence there is no shielding. The acoustic pressure due to the above source and Green's function becomes

$$p_{self}(\mathbf{x}', t) = \int_{t_1}\int_{\mathbf{y}} \hat{S}(\mathbf{x}', t; \mathbf{y}, t_1)\rho\frac{\partial^2(u_i u_j)}{\partial y_i \partial y_j}\,dt_1\,d\mathbf{y}. \tag{12}$$

$\hat{S}(\mathbf{x}', t; \mathbf{y}, t_1)$ is the inverse Fourier transform of $S(\mathbf{x}', \mathbf{y}, \Omega)e^{-i\Omega t_1}$,

$$\hat{S}(\mathbf{x}', t; \mathbf{y}, t_1) = \frac{1}{2\pi}\int_{-\infty}^{+\infty} S(\mathbf{x}', \mathbf{y}, \Omega)e^{-i\Omega(t-t_1)}\,d\Omega. \tag{13}$$

Upon transferring the derivatives from the source to the Green's function and making the approximation that variation of the magnitude of the Green's function $S(\mathbf{x}', \mathbf{y}, \Omega)$ with respect to the separation vector $\boldsymbol{\xi}$ within the source region is negligible compared to that of its phase, Eq. (12) leads to

$$\overline{p^2_{self}}(\mathbf{x}|\omega) = \int_{\mathbf{y}} |S_{,ij}(\mathbf{x}', \mathbf{y}, \Omega)S_{,kl}(\mathbf{x}', \mathbf{y}, \Omega)|I_{ijkl}(\mathbf{y}, \Omega)\,d\mathbf{y}. \tag{14}$$

Subscripts on S refer to derivatives with respect to source co-ordinate $\mathbf{y}$, and the phase factor $e^{-i\mathbf{k}.\boldsymbol{\xi}}$ is now included with the source correlation I_{ijkl}. In addition, the mean density gradients have been neglected so that density ρ is included within the source correlation function

$$I_{ijkl}(\mathbf{y}, \Omega) = \rho^2\int_{\boldsymbol{\xi}}\int_{-\infty}^{+\infty} \overline{(u_i u_j)(u'_k u'_l)}e^{-i\mathbf{k}.\boldsymbol{\xi}}e^{i\Omega\tau}\,d\tau\,d\boldsymbol{\xi}. \tag{15}$$

The volume integration in Eq. (14) usually includes the most energetic parts of the jet. For axisymmetric jets, the directivity factor may be averaged azimuthally with respect to source and observer circumferential angles to obtain a ring-source directivity factor a_{ijkl}. Subsequently, jet volume integration will be limited to radial and axial co-ordinates:

$$a_{ijkl} \equiv \frac{1}{4\pi^2}\int_{-\pi}^{+\pi}\int_{-\pi}^{+\pi} |S_{,ij}S_{,kl}|\,d\varphi\,d\varphi_o, \tag{16}$$

$$\overline{p^2}(\mathbf{x}|\omega) = \int_{y_1} \int_r a_{ijkl} I_{ijkl}(\mathbf{y}, \Omega)(2\pi r \, \mathrm{d}r \, \mathrm{d}y_1). \tag{17}$$

Eq. (17) is now written in an expanded form for a unit volume of turbulence at source point $\mathbf{y}$:

$$\begin{aligned}\sum (SelfNoise) = {} & I_{1111}a_{1111} + I_{2222}a_{2222} + I_{3333}a_{3333} + 2I_{1122}a_{1122} + 4I_{1212}a_{1212} \\ & + 2I_{1133}a_{1133} + 4I_{1313}a_{1313} + 2I_{2233}a_{2233} + 4I_{2323}a_{2323}.\end{aligned} \tag{18}$$

Directivity factors a_{ijkl} and shielding coefficients β are defined in Appendix A. In axisymmetric jets, $a_{2222} = a_{3333}$, $a_{1212} = a_{1313} = a_{1122} = a_{1133}$ and $a_{2233} = a_{2323}$. At 90°, Eq. (18) simplifies to

$$\sum (SelfNoise) = 2I_{2222}a_{2222} + 2(I_{2233} + 2I_{2323})a_{2233}, \quad \theta = 90^\circ. \tag{19}$$

At this point, a physics-based modelling approach is employed to obtain closed-form expressions for the various correlation coefficients appearing in Eqs. (18) and (19). For convenience, it is assumed that the joint probability distribution of velocities u and u' at points $\mathbf{y}$ and $\mathbf{y}'$ (separated in space and time) is normal, hence the fourth order cross-correlation function is written as a superposition of second order correlations [16]. In addition, the second order correlation is assumed separable, i.e., $\overline{u_i u'_j} = R_{ij}(\boldsymbol{\xi})\Psi(\tau)$. Here $R_{ij}(\boldsymbol{\xi})$ and $\Psi(\tau)$ denote the spatial and temporal parts of the correlation, respectively. From Eq. (15), the axial correlation coefficient becomes

$$I_{1111}(\mathbf{y}, \Omega) = 2\rho^2 G(\Omega) \int_{\boldsymbol{\xi}} R_{11}^2(\boldsymbol{\xi}) \mathrm{e}^{-\mathrm{i}\mathbf{k}.\boldsymbol{\xi}} \, \mathrm{d}\boldsymbol{\xi}, \quad G(\Omega) \equiv \int_{-\infty}^{+\infty} \Psi^2(\tau) \mathrm{e}^{\mathrm{i}\Omega\tau} \, \mathrm{d}\tau. \tag{20}$$

In homogeneous isotropic turbulence, the two-point correlation function has the form [13]

$$R_{ij}(\boldsymbol{\xi}) = \overline{u_1^2}\left[\left(f + \tfrac{1}{2}\xi f'\right)\delta_{ij} - \tfrac{1}{2} f' \xi_i \xi_j / \xi\right]. \tag{21}$$

In the following discussion both Gaussian and exponential spatial functions are examined.

2.2. Compact eddy approximation

In a compact eddy approximation, the assumption is made that the eddy length-scale ℓ is much shorter than the wavelength of the acoustic disturbances, i.e. $\omega\ell/a_\infty$ is small compared to unity. As such the factor $\mathrm{e}^{-\mathrm{i}\mathbf{k}.\boldsymbol{\xi}}$ is set equal to unity, which practically amounts to setting the wave number equal to zero. Thus the four-dimensional transform (15) simplifies:

$$I_{ijkl}(\mathbf{y}, \Omega) \cong \rho^2 \int_{\boldsymbol{\xi}} \int_{-\infty}^{+\infty} \overline{(u_i u_j)(u'_k u'_l)} \mathrm{e}^{\mathrm{i}\Omega\tau} \, \mathrm{d}\tau \, \mathrm{d}\boldsymbol{\xi}, \quad \text{(compact eddy)}. \tag{22}$$

Using an appropriate model in Eq. (20) with $k = 0$ one finds

$$\begin{aligned}
&\text{(a)} \quad I_{1111}(\mathbf{y},\Omega) = \frac{1}{2\sqrt{2}}\rho^2(\overline{u_1^2})^2\ell^3 G(\Omega), && f(\boldsymbol{\xi}) = \mathrm{e}^{-\pi\,\xi^2/\ell^2};\\
&\text{(b)} \quad I_{1111}(\mathbf{y},\Omega) = \frac{4}{5\pi^2}\rho^2(\overline{u_1^2})^2\ell^3 G(\Omega), && f(\boldsymbol{\xi}) = \mathrm{e}^{-\pi\,\xi/\ell};\\
&\text{(c)} \quad I_{1111}(\mathbf{y},\Omega) = \frac{1}{2\sqrt{2}}\rho^2(\overline{u_1^2})^2\ell_1\ell_2^2\, G(\Omega), && f(\boldsymbol{\xi}) = \mathrm{e}^{-\pi(\xi_1^2/\ell_1^2+\,\xi_{23}^2/\ell_2^2)};\\
&\text{(d)} \quad I_{1111}(\mathbf{y},\Omega) = \frac{4}{5\pi^2}\rho^2(\overline{u_1^2})^2\ell_1\ell_2^2\, G(\Omega), && f(\boldsymbol{\xi}) = \mathrm{e}^{-\pi\sqrt{(\xi_1^2/\ell_1^2+\xi_{23}^2/\ell_2^2)}};
\end{aligned} \tag{23}$$

with $\xi_{23}^2 = \xi_2^2 + \xi_3^2$. Models (a) and (b) assume isotropic turbulence, whereas (c) and (d) use an axisymmetric turbulence constructed from a set of kinematically compatible scalar functions [8]. Length-scales ℓ_1 and ℓ_2 are proportional to $(\overline{u_1^2})^{3/2}/\varepsilon$ and $(\overline{u_2^2})^{3/2}/\varepsilon$, respectively.

Consider the isotropic model, cases (a) and (b). Substituting the remaining correlation coefficients into Eq. (19) (see Appendix B) leads to

$$\sum(SelfNoise) = 2(a_{2222} + a_{2233})I_{1111}, \quad \theta = 90^\circ. \tag{24}$$

The shielding coefficients β that multiply the directivity factor a_{ijkl} result in noise attenuation within the zone of silence. At 90° emission angle, $\Omega = \omega$, and the shielding function is $g^2(r,\theta) = (a_\infty/a)^4$, where a is the sound speed at the source. Here $g^2(r,\theta)$ has no zero crossing, therefore there is no turning point and $\beta = 1$:

$$\sum(SelfNoise) = |S|^2k^4\left(\frac{a_\infty}{a}\right)^4 I_{1111}, \quad \theta = 90^\circ. \tag{25}$$

Away from 90°, Eq. (18) should be used directly. In addition, the shear noise contribution needs to be included as described in Ref. [8]. Model (c) shows that the directivity of jet noise with respect to its level at 90° is a function of anisotropy of turbulence [8].

Let τ_o be the inverse of the characteristic source frequency, which is proportional to turbulence kinetic energy and its dissipation rate as $\tau_o^{-1} = \Omega_o = \alpha_1\varepsilon/\kappa$. The eddy length-scale is obtained from $\ell \sim \tau_o u_1$. At this the point noise spectrum at 90° may be calculated using models (a) or (b) in Eq. (25) and an appropriately selected proportionality factor for ℓ. It is clear that the spectral shape will be the same for both models. For instance, if the proportionality factor selected for length-scale ℓ in model (b) was larger than that of model (a), say by factor $(5\pi^2/8\sqrt{2})^{1/3}$, then identical spectra are obtained.

Upon examining the three-dimensional energy spectrum for a two-point correlation $R_{ij}(\boldsymbol{\xi})$ using models (a) and (b), it is found that both scale as fourth power of spatial wave number when the wavelength is large. However, in the inertial sub-range, their decay rate is substantially different. The energy spectrum function, normalized with respect to $(1.5\overline{u_1^2})$, is given as (see page 208 of Ref. [13])

$$E(k) = \frac{\ell}{12\pi}\frac{(k\ell)^4}{(4\pi)^2}\mathrm{e}^{-\,(k\ell)^2/(4\pi)}, \quad f(\boldsymbol{\xi}) = \mathrm{e}^{-\pi\,\xi^2/\ell^2};$$

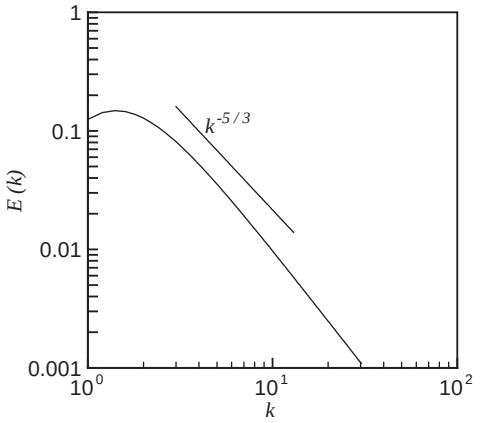

Fig. 1. Energy spectrum for the exponential function $f(\boldsymbol{\xi}) = \exp(-\pi\xi/\ell)$.

$$E(k) = \frac{16\ell}{3\pi^2}\frac{(k\ell/\pi)^4}{(1+k^2\ell^2/\pi^2)^3}, \quad f(\boldsymbol{\xi}) = \mathrm{e}^{-\pi\,\xi/\ell}. \tag{26}$$

Fig. 1 shows that the energy spectrum for the exponential function (model (b)) decays as k^{-2} at large wave number. This is reasonably close to the proposed Kolmogoroff's $k^{-5/3}$ scaling law [13]. Model (a), however, presents a much faster decay rate. These comparisons suggest that when non-compactness effects are accounted for, the two models, if properly used, should produce different spectral decay at high frequency (this will be shown in Section 2.4).

Ref. [13] argues that the exponential function may not be strictly correct on the grounds that (1) it is not parabolic at its vertex, (2) the lateral correlation $\overline{u_1 u_1'}$ with $\boldsymbol{\xi}$ in direction of ξ_2 remains positive for all ξ_2; whereas the correct curve must become negative for large ξ_2. Recent measurements of Bridges and Wernet [17] appear to suggest that the exponential spatial function provides a better fit to data relative to the Gaussian function (see Fig. 2).

2.3. Source non-compactness

Here the effect of source non-compactness on noise spectra is examined using Gaussian and exponential models (a) and (b). To carry out the integration with respect to $\boldsymbol{\xi}$ in Eq. (15) or (20), a convenient coordinate transformation has one of the axes ξ_i aligned with vector $\mathbf{k}$. In a spherical co-ordinate $\boldsymbol{\xi} = \xi(\cos\alpha, \sin\alpha\cos\varphi, \sin\alpha\sin\varphi)$, ξ_1 is aligned with wave number $\mathbf{k}$ such that $\mathbf{k}.\boldsymbol{\xi} = k\xi\cos\alpha$. Equivalently, one might select a cylindrical co-ordinate system $\boldsymbol{\xi} = (\xi_1, r\cos\varphi, r\sin\varphi)$ with ξ_1 in the direction of $\mathbf{k}$ such that $\mathbf{k}.\boldsymbol{\xi} = k\xi_1$. In any event, when turbulence is isotropic, the final result should be independent of the direction of wave number $\mathbf{k}$. Now with $f(\boldsymbol{\xi}) = \mathrm{e}^{-\pi\xi^2/\ell^2}$ one finds

$$I_{1111}(\mathbf{y},\Omega) = \frac{1}{2\sqrt{2}}\rho^2(\overline{u_1^2})^2\ell^3 G(\Omega)N(k\ell), \quad N(k\ell) = \mathrm{e}^{-k^2\ell^2/(8\pi)}, \tag{27}$$

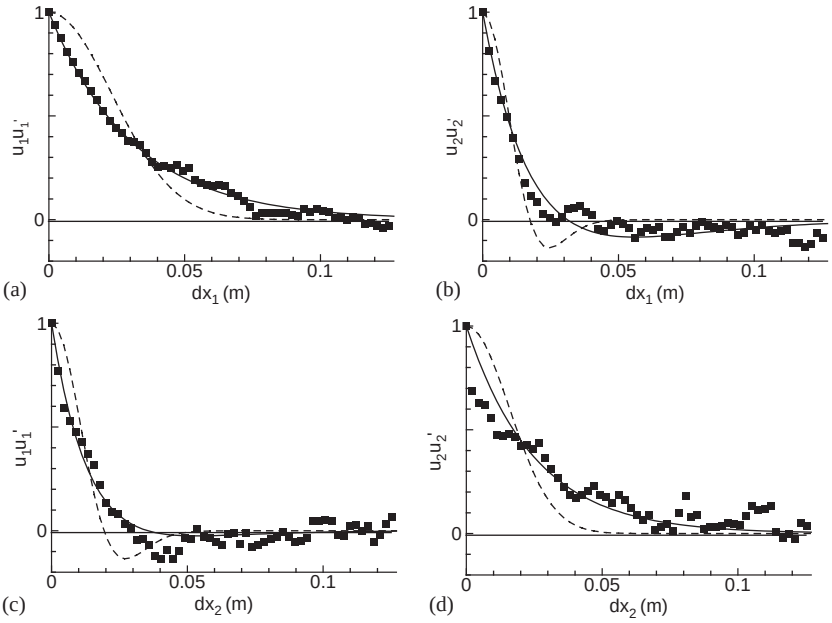

Fig. 2. Measurements of a two-point correlation in a high-subsonic jet: (a) $R_{11}(\xi_1)$, (b) $R_{22}(\xi_1)$, (c) $R_{11}(\xi_2)$, (d) $R_{22}(\xi_2)$. —, Eq. (21) with exponential spatial function; ----, Eq. (21) with the Gaussian function; ■, data.

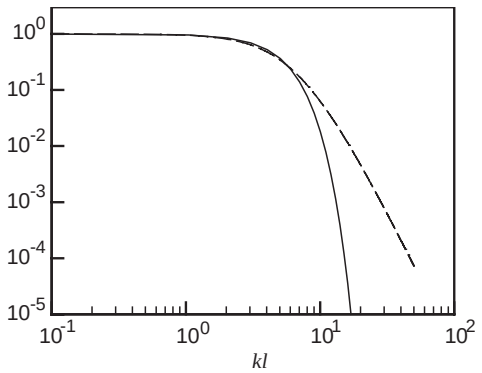

Fig. 3. Non-compactness factor $N(k\ell)$ for two types of spatial functions: —, Gaussian spatial function; ----, exponential function.

where $N(k\ell)$ denotes the non-compactness factor. Using an exponential function $f(\boldsymbol{\xi}) = \mathrm{e}^{-\pi\,\xi/\ell}$ leads to

$$I_{1111}(\mathbf{y},\Omega) = \frac{4}{5\pi^2}\rho^2(\overline{u_1^2})^2\ell^3 G(\Omega)N(k\ell),$$

$$N(k\ell) = 20\left(\frac{\pi}{k\ell}\right)^5\left[3\tan^{-1}\left(\frac{k\ell}{2\pi}\right) - 2\frac{k\ell}{\pi}\frac{5(k\ell/\pi)^2+12}{((k\ell/\pi)^2+4)^2}\right]. \tag{28}$$

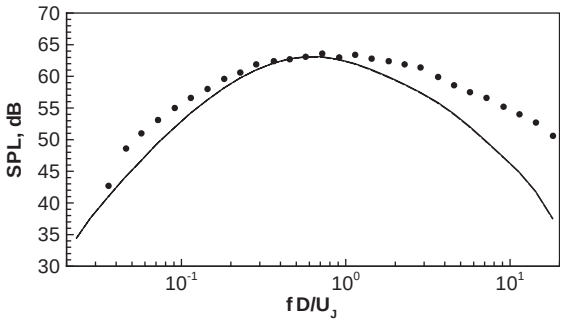

Fig. 4. MGBK noise spectra for Mach 0.5 cold jet at $\theta = 90^\circ$ using source model (a): —, compact source; ----, non-compact source; •, data.

Applying the law of limits repeatedly, the last expression for $N(k\ell)$ becomes 1 as $k\ell$ approaches zero. Fig. 3 shows that the non-compactness factors equal 1.0 for $0 \leqslant k\ell < 2$ and decays rapidly for $k\ell > 7$. The Gaussian function appears to produce a faster-decaying non-compactness factor. The above non-compactness factors repeat for other correlation coefficients as noted in Appendix B.

Since $\ell \sim \tau_o u_1$, one finds $k\ell \sim (\omega\tau_o)(u_1/a_\infty)$. The ratio u_1/a_∞ is usually smaller than 1.0 (of the order of 0.2 for the more energetic parts of the jet). In a compact eddy approximation $k\ell$ was assumed small hence $N(k\ell)$ was set equal to 1.0 for the entire range of the wave number. As frequency ω becomes very large, $\omega\tau_o$ may be large enough to reduce N below 1.0 (Fig. 3). Implications are that the effect of $N(k\ell)$ on spectra, if any, should be a slower decay rate at high frequency for the exponential function relative to the Gaussian. It is also evident that either model should produce a faster decay at high frequency when sources become non-compact. However, as will be seen shortly, these effects are visible only in the context of the spectral shape function $G(\Omega)N(k\ell)$. If $G(\Omega)$ has already decayed far enough before $N(k\ell)$ takes effect, then both models produce identical spectra.

Fig. 4 shows the MGBK prediction using Gaussian-isotropic source model (a). The effect of source non-compactness on predicted noise spectra for a Mach 0.5 cold jet is of the order of 0.12 dB at the high end of the spectra. Here the temporal part of the correlation was selected as [8]

$$\Psi(\tau) = \exp\left\{-\sqrt{(\sigma/2)^2 + (\tau/\tau_o)^2}\right\}. \tag{29}$$

The constant $\sigma = 0.8$, as was originally proposed in Ref. [8]. One might expect a similar effect at other angles, as $N(k\ell)$ is a common factor throughout Eq. (18).

Next the MGBK spectral shape function is explored.

2.4. Spectral shape function

Apart from factor k^4, which appears due to transfer of derivatives from the source to the Green's function (not included in the following discussion), the spectral shape function, denoted as $\hat{F}_1(\omega\tau_o)$, is simply the product $G(\Omega)N(k\ell)$. Function $G(\Omega)$ is obtained from

Eqs. (20) and (29):

$$\hat{F}_1(\omega\tau_o) = \sigma\tau_o \frac{K_1\left[\sigma\sqrt{1+(\Omega\tau_o/2)^2}\right]}{\sqrt{1+(\Omega\tau_o/2)^2}} N(k\ell). \tag{30}$$

The normalized spectral function becomes

$$\hat{F}_1(\omega\tau_o) = \frac{K_1\left[\sigma\sqrt{1+(\Omega\tau_o/2)^2}\right]}{\sqrt{1+(\Omega\tau_o/2)^2}K_1(\sigma)} N(k\ell), \quad \Omega = \omega(1 - M_c\cos\theta). \tag{31}$$

As σ becomes very small one finds

$$\hat{F}_1 = \frac{1}{1+(\Omega\tau_o/2)^2} N(k\ell), \quad \text{as } \sigma \to 0. \tag{32}$$

Fig. 5 shows the spectral shape function $\hat{F}_1(\omega\tau_o)$ for model (a), with $\ell/(U\tau_o) = 0.20$ which applies to the more energetic parts of the flow. Fig. 5(a) shows a negligible role for the non-compactness factor at $\sigma = 0.80$. The effect of $N(k\ell)$ becomes evident as shown in Figs. 5(b) and (c). It should be noted that when $\sigma \to 0$ the compact source model becomes increasingly inadequate (resulting in unusually high level of noise at high frequency).

Comparison of the spectral shape functions of models (a) and (b) shows a slower high-frequency decay for the exponential model (Figs. 6(a) and (b)). Shown in Fig. 7 is the predicted spectrum for the Mach 0.5 cold jet with $\sigma = 0$, including the non-compactness. Model (b) predicts a broader spectrum and noticeable high-frequency improvement relative to model (a). Here, the

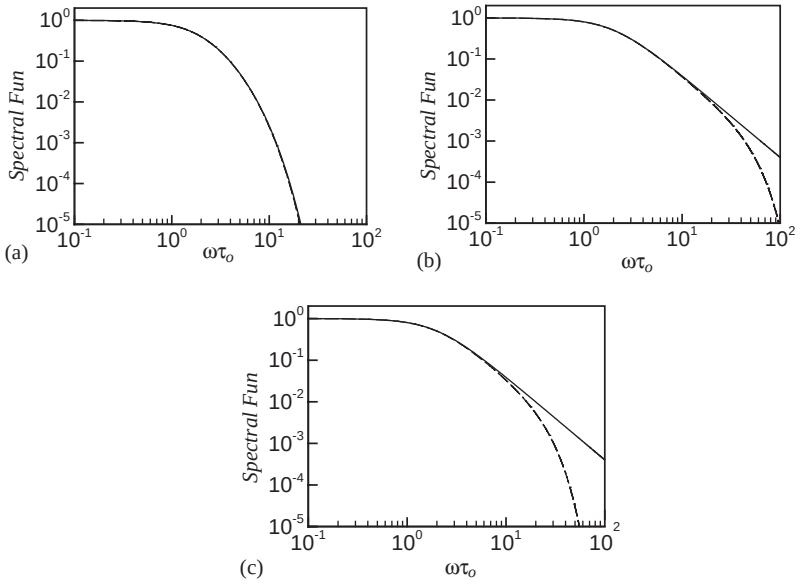

Fig. 5. Effect of source non-compactness on spectral shape of model (a): —, compact source; ----, non-compact source. (a) $U/a_\infty = 0.50$ or 1.0, $\sigma = 0.80$; (b) $U/a_\infty = 0.50$, $\sigma = 0.0$; and (c) $U/a_\infty = 1.0$, $\sigma = 0.0$.

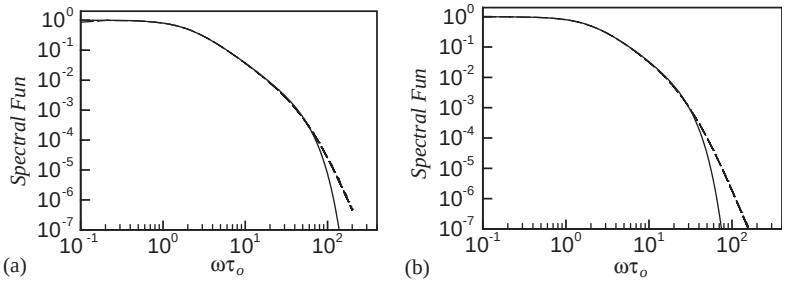

Fig. 6. Spectral shape function for a non-compact source at $\sigma = 0.0$: —, Gaussian spatial function; - - - -, exponential function. (a) $U/a_\infty = 0.50$, and (b) $U/a_\infty = 1.0$.

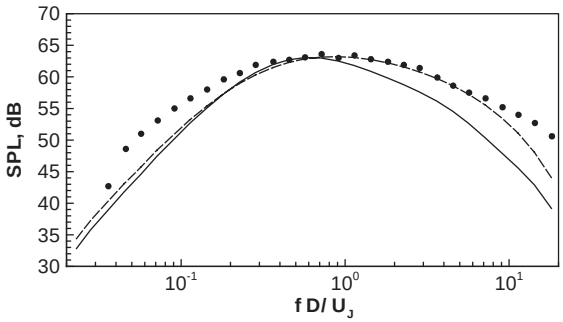

Fig. 7. MGBK noise spectra for Mach 0.5 cold jet at $\theta = 90^\circ$ with a non-compact source model and $\sigma = 0.0$: —, model (a); - - - -, model (b); •, data.

location of the peak frequency was adjusted slightly by selecting the proportionality constant α_1 defined in ($\tau_o^{-1} = \alpha_1 \varepsilon/\kappa$) as 0.225 and 0.170 for model (a) and (b) respectively.

3. Tam and Auriault's model

In Ref. [9] Tam and Auriault compute the fine-scale turbulence noise from an equation similar to Eq. (7). Here the Green's functions as well as the source cross correlation functions between the MGBK model and Tam's approach are compared.

3.1. Green's function

The Green's function to linearized Euler equations for a locally parallel flow is the solution to

$$L(G\mathrm{e}^{-\mathrm{i}\omega t}; U, x_1) = \mathrm{e}^{-\mathrm{i}\omega t}\delta(\mathbf{x} - \mathbf{x}_o), \tag{33}$$

where ω denotes source frequency with respect to stationary frame $\mathbf{x}$, $\mathbf{x}_o$ is the source location (same as $\mathbf{y}$), and L is Lilley's operator. Tam and Auriault [18] recast the problem into an adjoint operator for the adjoint Green's function G_a, which is related to the Green's function G of the original problem by a simple switch of the source and observer locations $\mathbf{x}_o$ and $\mathbf{x}$. The final result

for an axisymmetric mean flow (now multiplied by $2\pi a_\infty^2$ to compare with the high-frequency solution) is given as

$$G(\mathbf{x},\mathbf{x}_o,\omega) = G_a(\mathbf{x}_o,\mathbf{x},\omega),$$
$$G_a(\mathbf{x}_o,\mathbf{x},\omega) = \frac{e^{-ik(x\cos\theta - R)}}{4\pi k a_\infty R}\sum_{m=0}^{\infty} f_m(r,k,\theta)\cos m\varphi, \quad r_o \leqslant R_o. \tag{34}$$

Function f_m is obtained by solving a second order ordinary differential equation [18] and matching the inner solution (34) with the outer solution at the jet boundary R_o which is obtained by solving the Helmholtz equation,

$$G_a(\mathbf{x}_o,\mathbf{x},\omega) = \frac{e^{-ik(x\cos\theta - R)}}{4\pi k a_\infty R}\sum_{m=0}^{\infty} [(-i)^m \varepsilon_m J_m(\chi) + A_m H_m^{(1)}(\chi)]\cos m\varphi, \quad r_o \geqslant R_o, \tag{35}$$

where $\chi = kR_o \sin\theta$. A numerical solution to this differential equation is obtained for a selected observer angle θ and frequency ω. In addition, the mean velocity and temperature profiles at the stream-wise source location need to be specified through a RANS solver. The number of summation modes m required for a converged solution (34) increases with frequency ω.

The corresponding high-frequency solution [15,19] for a non-convecting ($\Omega = \omega$) monopole type source takes one of the following forms depending on the location of the source r_o relative to the zero crossing point r_σ of the shielding function, i.e., $g(r_\sigma,\theta) = 0$ (see Appendix A for the definition of g):

$$G(\mathbf{x},\mathbf{y},\omega) = \frac{i}{4\pi a_\infty kR}\frac{a_o/a_\infty}{(1-M_o\cos\theta)^2}\left(\frac{\zeta_o}{r_o f_o}\right)^{1/2} e^{ikR} e^{ik\left[\int_{r_\sigma}^{\infty}(g-g_\infty)\,dr - g_\infty r_\sigma\right]} \times e^{-k[\zeta_\sigma - \zeta_o\cos(\varphi-\varphi_o)]}, \quad r_o < r_\sigma, \tag{36}$$

with $f^2 = -g^2$, $\zeta = \int_0^r f(r,\theta)\,dr$, or

$$G(\mathbf{x},\mathbf{y},\omega) = \frac{i}{4\pi a_\infty kR}\frac{a_o/a_\infty}{(1-M_o\cos\theta)^2}\left(\frac{\zeta_o}{r_o g_o}\right)^{1/2} e^{ikR} e^{ik\left[\int_0^{\infty}(g-g_\infty)\,dr - \zeta_o\cos(\varphi-\varphi_o)\right]}, \quad r_o > r_\sigma, \tag{37}$$

with $\zeta = \int_0^r g(r,\theta)\,dr$.

Figs. 8–11 compare the above Green's functions (normalized with respect to the free-space Green's function) for a stationary ring source at seven diameters from the jet exit ($x/D = 7$). The mean flow was calculated numerically for a convergent jet at Mach 0.9 and temperature ratio of 1.0 by solving Reynolds-averaged Navier–Stokes equations with a standard $\kappa - \varepsilon$ turbulence model. Green's function comparisons are shown for a range of Strouhal numbers ($St = fD/U_j$) and ring source radii (r_o/D). The agreement is generally good at high frequency. As the Strouhal number is lowered, the high-frequency approximation appears to deteriorate. Discrepancies become increasingly visible near the boundary of the zone of silence, with the numerical Green's function predicting a larger zone of silence. In the neighborhood of $\theta = 90^\circ$, however, there is good agreement between the two Green's functions. Since the spectral peak for both Mach 0.5 and 0.9 cold jets is near $St = 0.9$, the high-frequency solution should be adequate for noise prediction at and near 90°.

It is noted that the Green's function for a monopole type source scales as k^{-1} with respect to the wave number and as $1/(1 - M_o\cos\theta)^2$ with respect to the polar angle.

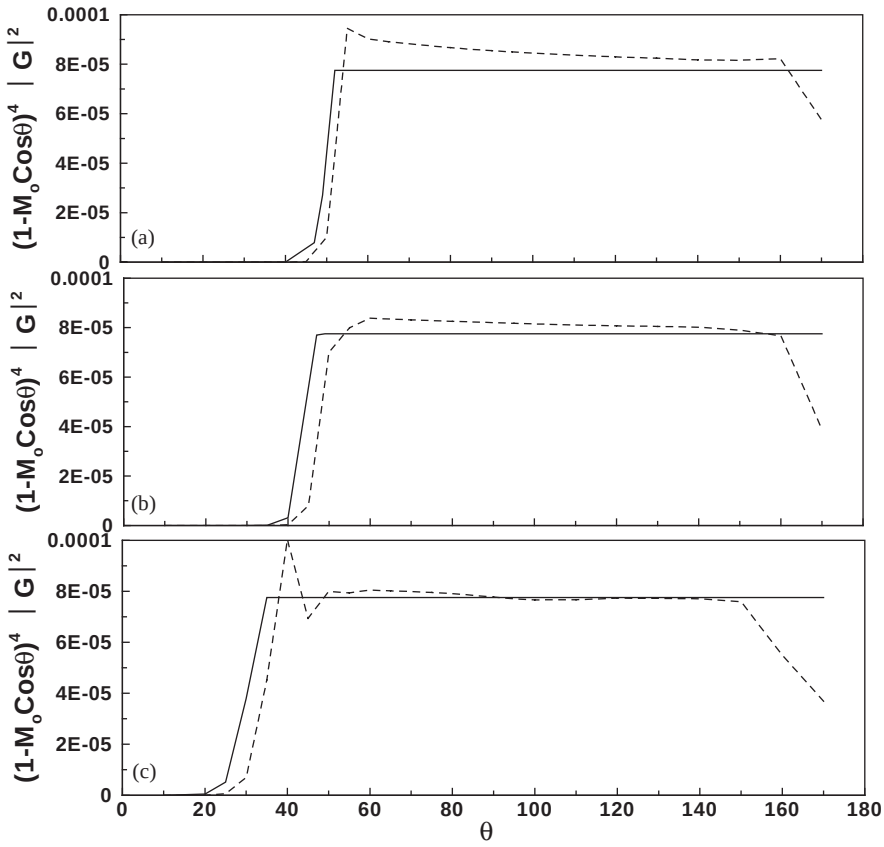

Fig. 8. Comparison between the high frequency Green's function (solid lines) and the numerically calculated Green's function (dashed lines) for a stationary ring source at $St = 5.0$ and radius of: (a) $r_o/D = 0.31$; (b) $r_o/D = 0.50$; and (c) $r_o/D = 0.90$.

3.2. Source model

Tam and Auriault [9] propose a two-point, fourth order, axial velocity correlation in a fixed reference frame,

$$\left\langle \frac{Dq_s(\mathbf{x}_1,t_1)}{Dt_1}\frac{Dq_s(\mathbf{x}_2,t_2)}{Dt_2}\right\rangle = \frac{\hat{q}_s^2}{c^2\tau_s^2}\exp\left\{\frac{-|\xi_1|}{U\tau_s} - \frac{\ln 2}{\ell_s^2}[(\xi_1 - U\tau)^2 + \xi_{23}^2]\right\}, \tag{38}$$

with $\boldsymbol{\xi} = \mathbf{x}_1 - \mathbf{x}_2$, $\tau = t_1 - t_2$, ξ_{23} as defined earlier, and U is the mean velocity at the source location, which can be replaced with the source convection velocity and the source strength q is proportional to the turbulence kinetic energy of fine-scale turbulence. Subscript s denotes the source location and $\boldsymbol{\xi}$ here is used as separation vector in a fixed reference frame.

The corresponding axial correlation coefficient used in the MGBK describes the cross correlation of the Reynolds stress components rather than their convective derivatives. Following

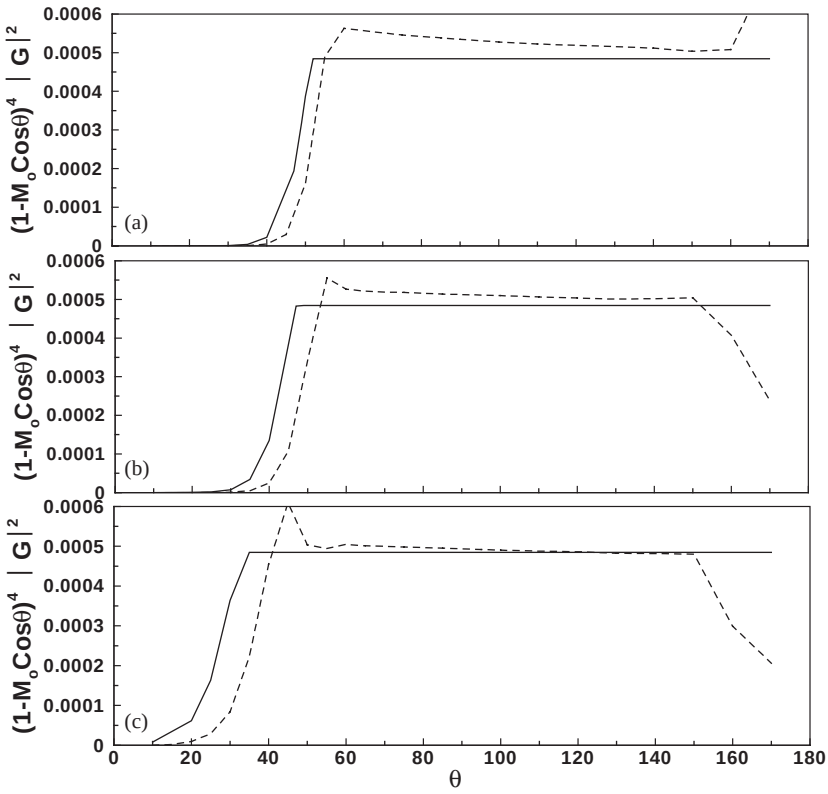

Fig. 9. As Fig. 8 but for $St = 2.0$.

the usual MGBK methodology, the fourth order correlation $I_{1111}(\xi,\tau) = \langle(\rho u_1 u_1)(\rho u_1' u_1')\rangle$ is expressed as a sum of second order tensors. The element of I_{1111} contributing to the noise field is simply $2R_{11}^2(\boldsymbol{\xi})\Psi^2(\tau)$ which, upon using model (a) in Eq. (21), and making a transition to a fixed reference frame, becomes

$$I_{1111}(\boldsymbol{\xi},\tau) = 2\rho^2(\overline{u_1^2})^2\left(1-\frac{\pi}{\ell^2}\xi_{23}^2\right)^2 \exp\left\{-2\frac{\pi}{\ell^2}[(\xi_1 - U\tau)^2 + \xi_{23}^2]\right\}\Psi^2(\tau), \tag{39}$$

and the temporal function is given by Eq. (29).

The factor $(1-\pi\xi_{23}^2/\ell^2)$ in Eq. (39) reduces $I_{1111}(\boldsymbol{\xi},\tau)$ to zero as the normalized lateral distance (ξ_{23}/ℓ) approaches $1/\sqrt{\pi}$. Beyond this point the correlation is practically zero.

In order to compare correlation functions (38) and (39) on an equal basis, suppose one relates time- and length scales and defines the dimensionless parameters

$$\ell = \left(\frac{2\pi}{\ln 2}\right)^{0.5}\ell_s, \quad \tau_o = 2\tau_s, \quad \bar{\xi}_i = \xi_i/\ell_s, \quad \bar{\tau} = \tau/\tau_s. \tag{40}$$

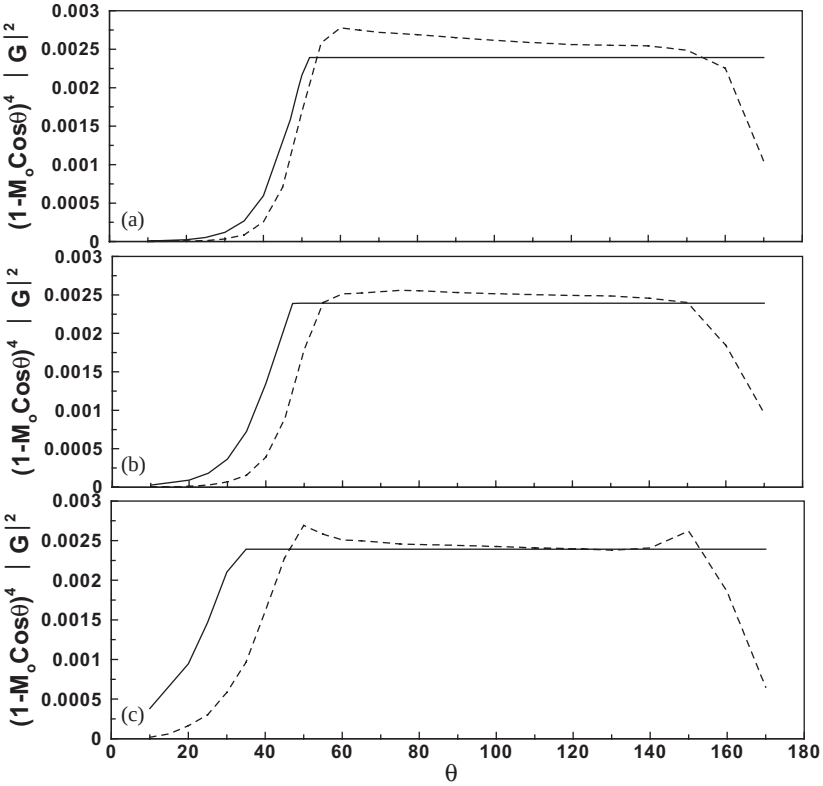

Fig. 10. As Fig. 8 but for $St = 0.90$.

Now the lateral correlations, with zero time-delay, and normalized in magnitude become

$$\left\langle \frac{Dq_s(x,t_1)}{Dt_1}\frac{Dq_s(x+\xi_{23},t_1)}{Dt_2}\right\rangle = \exp\{-\ln 2\,\bar{\xi}_{23}^2\} \tag{41}$$

and

$$I_{1111}(\xi_{23},0) = \left(1-\frac{\ln 2}{2}\bar{\xi}_{23}^2\right)^2 \exp\{-\ln 2\bar{\xi}_{23}^2\}. \tag{42}$$

Fig. 12 shows that Eqs. (41) and (42) decay somewhat differently. Tam and Auriault's correlation (41) does not have a zero intersect and decays at a slower rate. Limited data available on fourth-order correlation measurements [20] seem in better agreement with the MGBK model. However, this difference may practically be insignificant in noise prediction. An interested reader may find more information on the second-order lateral correlation in a book by Townsend [21].

Aside from ξ_{23}, which is now set equal to 0.0, the two models appear similar. The normalized axial cross correlation functions are

$$\left\langle \frac{Dq_s(x,t_1)}{Dt_1}\frac{Dq_s(x+\xi_1,t_2)}{Dt_2}\right\rangle = \exp\{-\alpha|\bar{\xi}_1| - \ln 2(\bar{\xi}_1-\bar{\tau}/\alpha)^2\}, \tag{43}$$

$$I_{1111}(\xi_1,\tau) = \exp\left\{-\sqrt{\sigma^2+\bar{\tau}^2} - \ln 2(\bar{\xi}_1-\bar{\tau}/\alpha)^2\right\} \tag{44}$$

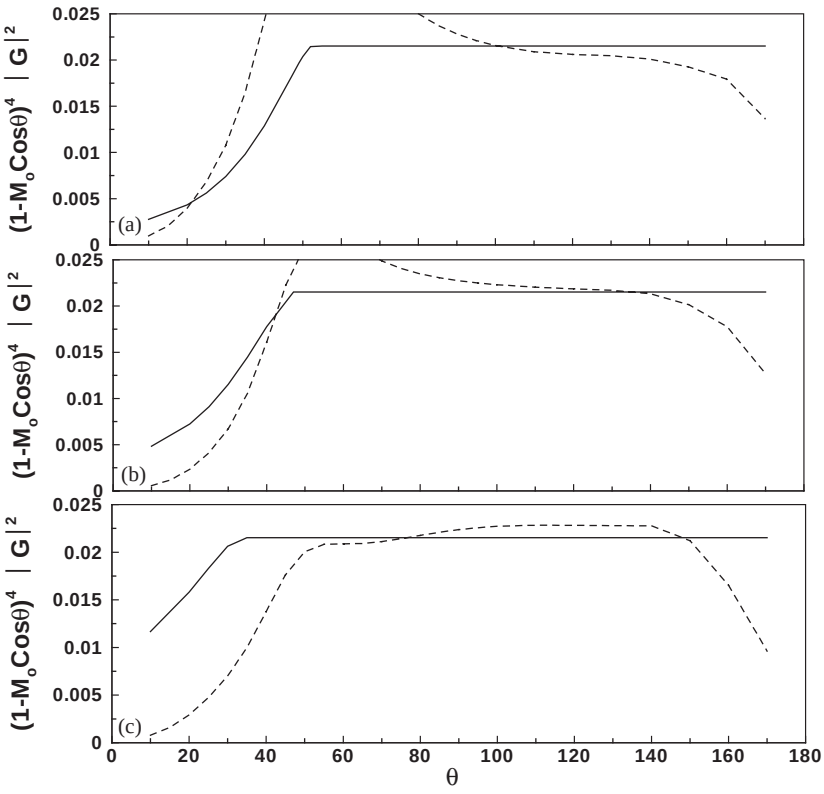

Fig. 11. As Fig. 8 but for $St = 0.30$.

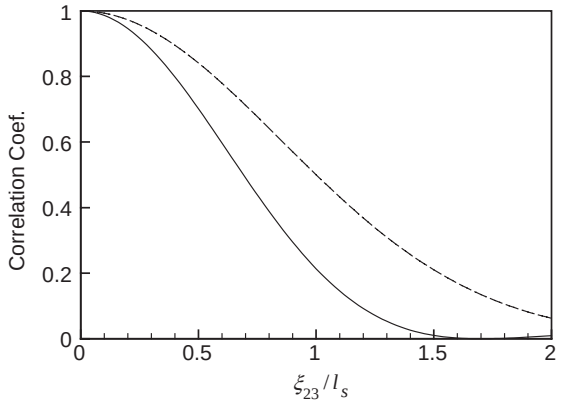

Fig. 12. Correlation coefficient $I_{1111}(\xi_{23})$: —, MGBK; ----, Tam et al.

with $\alpha = (\ell_s/U\tau_s)$. Using Tam and Auriault's constants ($\ell_s = c_\ell \kappa^{3/2}/\varepsilon, \tau_s = c_\tau \kappa/\varepsilon$, with $c_\ell = 0.256$, $c_\tau = 0.233$) one finds $\alpha = (c_\ell/c_\tau)(\kappa^{0.5}/U)$. Let's set U equal to the convection velocity $0.65U_J$. In the more energetic parts of the flow (mixing layer) one might select $(\kappa^{0.5}/U_J) \cong 0.12$, and find $\alpha \cong 0.20$.

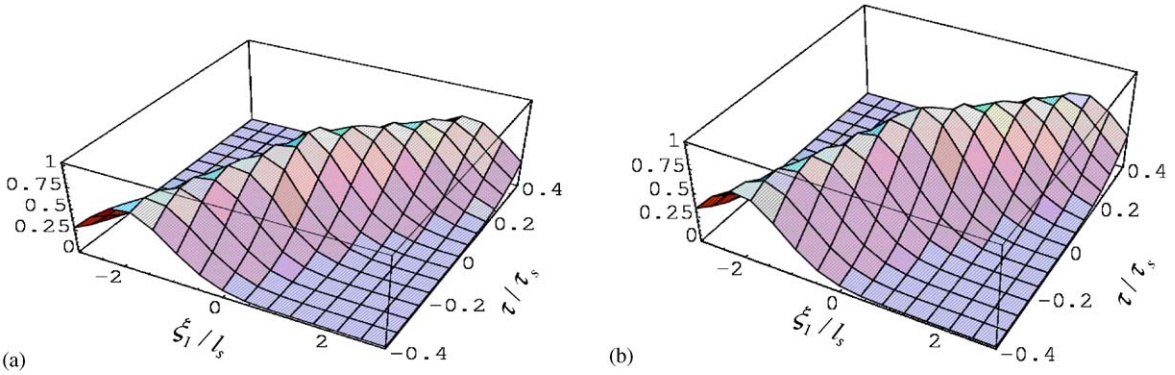

Fig. 13. Comparison between the axial cross-correlation coefficient of Tam et al. and MGBK: (a) Tam's model (Eq. (43)); (b) MGBK model (Eq. (44)) with $\sigma = 0$.

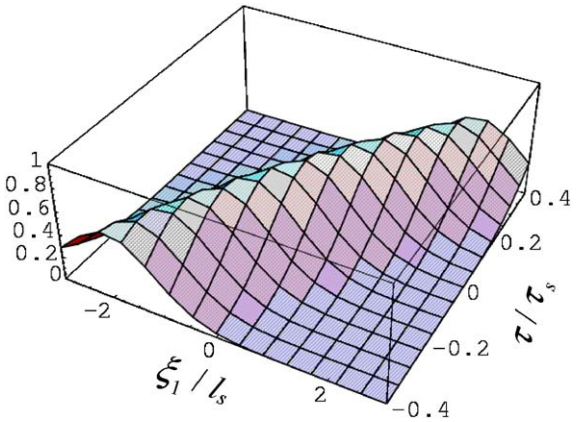

Fig. 14. MGBK cross correlation function (Eq. (44)) with $\sigma = 0.40$.

Fig. 13 shows Tam and Auriault's correlation coefficient (43) and the MGBK model (44), with $\sigma = 0$. The effect of the small parameter σ is shown in Fig. 14. Aside from the slight difference described above in comparing the lateral correlations, the two models exhibit similar features. Next, the spectral shape functions are compared.

3.3. Spectral function

The MGBK spectral function was written earlier in a moving frame as a Fourier transform of the temporal function $\Psi^2(\tau)$, multiplied by the non-compactness factor. In a fixed frame, the variable τ appears in $(\xi_1 - U\tau)$, hence the spatial function needs to be include in the integration. However, with a simple transformation $\boldsymbol{\xi}_m = \boldsymbol{\xi} - \mathbf{i}U\tau$, the spectral shape function (31)

is recovered. For comparison with Tam's spectra let $\tau_o = 2\tau_s$ as defined in Eq. (40):

$$\hat{F}_1(\omega\tau_s) = \frac{K_1\left[\sigma\sqrt{1+(\Omega\tau_s)^2}\right]}{\sqrt{1+(\Omega\tau_s)^2}K_1(\sigma)}N(k\ell), \quad \Omega = \omega(1-M_c\cos\theta). \tag{45}$$

$N(k\ell)$ for model (a) is given by Eq. (27). And

$$\hat{F}_1 = \frac{1}{1+(\Omega\tau_s)^2}N(k\ell), \quad \text{as } \sigma\to 0. \tag{46}$$

Following Eq. (33) of Ref. [9], Tam and Auriault's spectral function $\hat{F}_2$ is written for a unit volume of turbulence at $\mathbf{y}$:

$$\hat{F}_2(\omega\tau_s) = \int_\xi\int_\tau p_a(\mathbf{y},\mathbf{x},-\omega)p_a(\mathbf{y}+\boldsymbol{\xi},\mathbf{x},+\omega) \times \exp\left\{-\frac{|\xi_1|}{U\tau_s} - \frac{\ln 2}{\ell_s^2}[(\xi_1-U\tau)^2+\xi_{23}^2] + \mathrm{i}\omega\tau\right\}\mathrm{d}\tau\,\mathrm{d}\boldsymbol{\xi}. \tag{47}$$

Here p_a is the direct Green's function, which is obtained from switching source and observer locations in the adjoint problem. As was done earlier, the product of the Green's functions is approximated as the magnitude at the center of the correlation volume multiplied by a proper phase,

$$p_a(\mathbf{y},\mathbf{x},-\omega)p_a(\mathbf{y}+\boldsymbol{\xi},\mathbf{x},+\omega) \approx |p_a(\mathbf{y},\mathbf{x},-\omega)|^2 \mathrm{e}^{\mathrm{i}\mathbf{k}.\boldsymbol{\xi}}. \tag{48}$$

Phase factor $\mathbf{k}.\boldsymbol{\xi}$ should not carry a preferred direction since rays are emitted at all angles and the separation vector $\boldsymbol{\xi}$ may also take any direction. It follows that

$$\hat{F}_2(\omega\tau_s) = |p_a(\mathbf{y},\mathbf{x},-\omega)|^2\int_\xi\int_\tau \exp\left\{-\frac{|\xi_1|}{U\tau_s} - \frac{\ln 2}{\ell_s^2}[(\xi_1-U\tau)^2+\xi_{23}^2] + \mathrm{i}\mathbf{k}.\boldsymbol{\xi} + \mathrm{i}\omega\tau\right\}\mathrm{d}\tau\,\mathrm{d}\boldsymbol{\xi},$$

or upon integrating over τ,

$$\hat{F}_2(\omega\tau_s) = |p_a(\mathbf{y},\mathbf{x},-\omega)|^2\exp\left(-\frac{1}{\ln 2}\left(\frac{\omega\ell_s}{2U}\right)^2\right)\int_\xi \exp\left\{-\frac{|\xi_1|}{U\tau_s} - \frac{\ln 2}{\ell_s^2}\xi_{23}^2 - \mathrm{i}\frac{\omega\xi_1}{U} + \mathrm{i}\mathbf{k}.\boldsymbol{\xi}\right\}\mathrm{d}\boldsymbol{\xi}.$$

As before, make a co-ordinate transformation with respect to the dummy variable $\boldsymbol{\xi}$ such that ξ_1 aligns with $\mathbf{k}$ (i.e., $\mathbf{k}.\boldsymbol{\xi} = k\xi_1$). The component of U in direction of $\mathbf{k}$ becomes $U_\theta = U\cos\theta$, and

$$\hat{F}_2(\omega\tau_s) = |p_a(\mathbf{y},\mathbf{x},-\omega)|^2 2\ell^3\exp\left(-\frac{1}{\ln 2}\left(\frac{\omega\ell_s}{2U}\right)^2\right)\int_{-\infty}^{+\infty}\int_{-\infty}^{+\infty}\mathrm{d}\xi_2\,\mathrm{d}\xi_3 \times \int_0^\infty \exp\left\{-\frac{\ell\xi_1}{U_\theta\tau_s} - \ln 2\xi_{23}^2\right\}\cos\left[\left(\frac{\omega}{U_\theta}-k\right)\xi_1\right]\mathrm{d}\xi_1.$$

Next, transition to polar co-ordinates $\boldsymbol{\xi} = (\xi_1, r\cos\varphi, r\sin\varphi)$ results in

$$\hat{F}_2(\omega\tau_s) = |p_a(\mathbf{y},\mathbf{x},-\omega)|^2\frac{2\pi\ell_s^3}{\ln 2}\frac{U\tau_s/\ell_s}{1+(\omega\tau_s - U_\theta\tau_s k)^2}\exp\left(-\frac{1}{\ln 2}\left(\frac{\omega\ell_s}{2U}\right)^2\right). \tag{49}$$

Expression (49) is now normalized to obtain the spectral shape function. Here source definition requires that $p_a \sim k$. The magnitude of the Green's function is also taken out of the spectral function, as was done in Eq. (45). For a compact eddy ($k = 0$),

$$\hat{F}_2(\omega\tau_s) = \frac{1}{1+(\omega\tau_s)^2}\exp\left(-\frac{1}{\ln 2}\left(\frac{\omega\ell_s}{2U}\right)^2\right), \quad \text{(compact eddy)}, \tag{50}$$

and

$$\hat{F}_2(\omega\tau_s) = \frac{1}{1+(\omega\tau_s)^2\left(1-\frac{U}{a_\infty}\cos\theta\right)^2}\exp\left(-\frac{1}{\ln 2}\left(\frac{\omega\ell_s}{2U}\right)^2\right), \quad \text{(non-compact eddy)}. \tag{51}$$

This result is the same as that reported by Tam and Auriault [9] but was derived without resorting to the following approximation that was suggested in Ref. [9]:

$$p_a(\mathbf{y},\mathbf{x},-\omega)p_a(\mathbf{y}+\boldsymbol{\xi},\mathbf{x},+\omega) \cong |p_a(\mathbf{y},\mathbf{x},-\omega)|^2 e^{ik\xi_1\cos\theta}.$$

At this point let's compare Eq. (51) with the MGBK shape function (model (a)) given by Eq. (45). Fig. 15 shows comparisons with $\ell_s/U\tau_s = 0.20$ as was selected earlier. The MGBK spectral shape (with $\sigma = 0.20$) agrees quite favorably with Tam's results at $U/a_\infty = 0.325$ and 0.65 as shown in Figs. 15(a) and (b), corresponding to jet exit velocities of $U_J/a_\infty = 0.50$ and $U_J/a_\infty = 1.0$ respectively.

As noted before, wave number powers k^4 (MGBK model) and k^2 (Tam's model) were deliberately dropped (due to normalization with respect to Green's function) when comparing the spectral shape functions. In the MGBK approach, the factor k^4 appears when two spatial derivatives and one convective derivative are transferred from the source to the Green's function as seen in Eq. (25). Tam and Auriault, on the other hand, maintain that the convective derivative is included in their source modeling. As a result the Green's function p_a remains of the order of k (Eq. (28) of Ref. [18]), which incidentally indicates that source q_s should be of the quadrupole type. With the convective derivative now hidden in the source, the power spectral function becomes proportional to k^2.

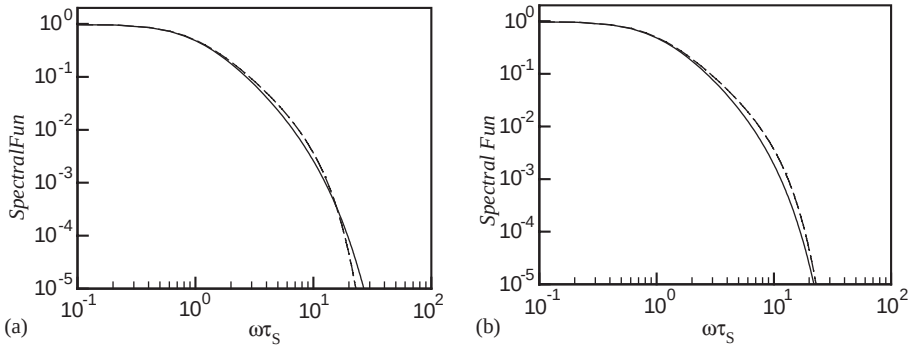

Fig. 15. Spectral shape functions at 90°; MGBK with $\sigma = 0.20$ (solid lines); Tam et al. (dashed lines): (a) $U/a_\infty = 0.325$, and (b) $U/a_\infty = 0.65$.

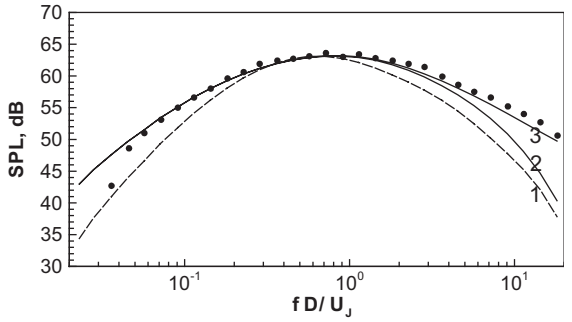

Fig. 16. Predictions for Mach 0.5 cold jet at 90° using a spectral shape function consistent with Tam et al.: (1) MGBK $\sim k^4$; (2) $\sim k^2$; (3) $\sim k^2$, no loss; •, data.

Morris and Farassat [22] described this in more detail in a recent paper and suggested that a consistent approach should result in $\sim k^4$ for both MGBK and Tam's analysis.

Fig. 16 shows the MGBK predictions for the Mach 0.5 cold jet using model (a) and a spectral shape function that matches that of Tam and Auriault's (curve 1). Predictions obtained by replacing the k^4 wave-number factor by k^2 (as in Tam and Auriault approach) are also shown. In doing so, some minor adjustments had to be made in the calibration constant related to the source characteristic frequency to preserve the location of the peak spectra. The noise spectrum naturally becomes broader with the k^2 factor (compare 1 and 2), and improvements are noticed at both ends.

Additional high-frequency improvement could be gained by simply removing the atmospheric attenuation built in the MGBK code from predictions and implying that it is built into the source model (as was done in the spectral predictions of Ref. [9] at $R/D = 100$). However, predicted the noise spectrum should account for atmospheric attenuation. This amounts to attenuating the high-frequency noise depending on the observer distance and atmospheric conditions (i.e., relative humidity and ambient temperature). Noise measurements usually reflect the atmospheric attenuation. Fig. 16 (curve 3) shows the significance of atmospheric loss on predicted spectra. Although excellent agreement with data is thereby obtained, two very questionable steps were taken to predict a better spectrum.

As was shown earlier (Fig. 7), good agreement with data could be achieved by selecting an exponential spatial function (model (b)) in place of the Gaussian function.

4. Conclusions

In the preceding discussions, alternative model representations for the two-point space–time correlation appearing in physics-based jet noise prediction methodologies were examined. It was argued that a proper representation of the source, consistent with the observations and accepted fundamentals related to turbulence statistics, should improve prediction of the flow-generated noise in the framework of Lilley's equation. The discussions centered on noise from small-scales of motion and at a 90° observer-angle. The main result of the study was described in Fig. 7. It was

shown that an exponential spatial function, with source non-compactness included, predicts a broader spectrum relative to a Gaussian function and better agreement with data. The effect of turbulence anisotropy may readily be accounted for by selecting model (d) of Section 2.2 as a non-compact source.

Away from 90°, mean-flow refraction effects as well as convective amplification due to source motion become crucial in capturing the peak directivity that occurs near the down-stream axis. A high-frequency approximation offers an analytical solution to the Green's function, but comparisons of Section 3.1 indicate that it might not be an appropriate approximation at the peak directivity angle and at small Strouhal numbers.

A numerically computed Green's function [18] provides extra flexibility at low frequency, at the cost of added numerical intensity.

Acknowledgements

The authors would like to thank Dr. Stewart Leib, NASA Glenn Research Center, for helpful comments in writing the manuscript. In addition, the authors wish to thank Dr. Srini Bhat, Boeing, for providing the jet noise data.

Appendix A. Quadrupole directivity factors

The directivity factor for various quadrupole source components (in the absence of mean density gradient) is

$$a_{1111} = \frac{\cos^4\theta}{(1-M_c\cos\theta)^4}\left(\frac{\Omega}{a_\infty}\right)^4|S|^2\beta, \quad a_{1122} = \frac{g^2(r_o)\cos^2\theta}{2(1-M_c\cos\theta)^2}\left(\frac{\Omega}{a_\infty}\right)^4|S|^2\beta,$$
$$a_{2222} = \tfrac{3}{8}g^4(r_o)\left(\frac{\Omega}{a_\infty}\right)^4|S|^2\beta, \quad a_{2233} = \tfrac{1}{8}g^4(r_o)\left(\frac{\Omega}{a_\infty}\right)^4|S|^2\beta \tag{A1}$$

and the shielding function is

$$g^2(r) = \frac{(1-M_o\cos\theta)^2(a_\infty/a)^2 - \cos^2\theta}{(1-M_c\cos\theta)^2}. \tag{A2}$$

It should be noted that correlation coefficients a_{ijkl} all have a Doppler factor to the power of 4 in the denominator, which when multiplied by $(\Omega/a_\infty)^4$ makes a_{ijkl} proportional to k^4. Shielding coefficients β depends on the number of turning points of $g^2(r)$ as well as the location of source point r_o with respect to that of the turning point r_σ. In general, the deeper the source is embedded in the negative region of $g^2(r)$, larger is the shielding. For example, when there is only one turning point the shielding becomes

$$\beta = \begin{cases} 1, & r_{\sigma_1} < r_o, \\ \exp\left\{-2\dfrac{\Omega}{a_\infty}\int_{r_o}^{r_{\sigma_1}}\sqrt{|g^2(r)|}\,\mathrm{d}r\right\}, & r_o < r_{\sigma_1}. \end{cases} \tag{A3}$$

When there are two turning points such that $r_{\sigma_2} < r_{\sigma_1}$ then

$$\beta = \begin{cases} 1, & r_{\sigma_1} < r_o, \\ \exp\left\{ -2\dfrac{\Omega}{a_\infty} \int_{r_o}^{r_{\sigma_1}} \sqrt{|g^2(r)|}\, \mathrm{d}r \right\}, & r_{\sigma 2} < r_o < r_{\sigma_1}, \\ \exp\left\{ -2\dfrac{\Omega}{a_\infty} \int_{r_{\sigma_2}}^{r_{\sigma_1}} \sqrt{|g^2(r)|}\, \mathrm{d}r \right\}, & r_o < r_{\sigma_2} < r_{\sigma_1}. \end{cases} \tag{A4}$$

The shielding function for cases involving more than two turning points can similarly be expressed.

Appendix B. Correlation coefficients

For a homogeneous isotropic turbulence, various correlation coefficients are related to the axial component by

$$I_{2222} = I_{3333} = I_{1111}, \quad I_{1122} = I_{1133} = I_{2233} = \tfrac{1}{8} I_{1111}, \quad I_{1212} = I_{1313} = I_{2323} = \tfrac{7}{16} I_{1111}. \tag{B1}$$

These relations hold with either Gaussian or exponential spatial functions and apply to compact as well as non-compact source models.

References

[1] J. Bridges, Measurements of turbulent flow field in separable flow nozzles with enhanced mixing devices—test report, NASA TM-2002-211366, 2002.

[2] J.B. Freund, Noise source in a low-Reynolds-number turbulent jet at Mach 0.9, *Journal Fluid Mechanics* 438 (2001) 277–305.

[3] P.J. Morris, E.T. Scheidegger, L.N. Long, Jet noise simulation for circular nozzles, AIAA Paper 2000-2080, 2000.

[4] R.R. Mankbadi, R. Hixon, Very large eddy simulations of jet noise, AIAA Paper 2000-2008, 2000.

[5] A. Uzan, G.A. Blaisdell, A.S. Lyrintzis, 3-D Large eddy simulation for jet aeroacoustics, AIAA Paper 2003-3322, 2003.

[6] C. Seror, P. Sagaut, C. Bailly, D. Juve, Subgrid-scale contribution to noise production in decaying isotropic turbulence, *American Institute of Aeronautics and Astronautics Journal* 38 (2000) 1795–1803.

[7] C. Bogey, C. Bailly, LES of a high Reynolds, high subsonic jet: effects of the inflow conditions on flow and noise, AIAA Paper 2003-3170, 2003.

[8] A. Khavaran, Role of anisotropy in turbulent mixing noise, *American Institute of Aeronautics and Astronautics Journal* 37 (1999) 832–841.

[9] C.K.W. Tam, L. Auriault, Jet mixing noise from fine-scale turbulence, *American Institute of Aeronautics and Astronautics Journal* 37 (1999) 145–153.

[10] R.H. Bush, G.D. Power, C.E. Towne, WIND: The production flow solver of the NPARC Alliance, AIAA Paper 98-0935, 1998.

[11] S.L. Woodruff, J.M. Seiner, M.Y. Hussani, G. Erlebacher, Implementation of new turbulence spectra in the Lighthill analogy source terms, *Journal of Sound and Vibration* 242 (2001) 197–214.

[12] A. Khavaran, E.A. Krejsa, C.M. Kim, Computation of supersonic jet mixing noise for an axisymmetric convergent-divergent nozzle, *Journal of Aircraft* 31 (1994) 603–609.

[13] J.O. Hinze, *Turbulence*, McGraw-Hill, New York, 1975.

[14] M.E. Goldstein, An exact form of Lilley's equation with a velocity quardupole/temperature dipole source term, *Journal of Fluid Mechanics* 433 (2001) 231–236.

[15] R. Mani, P.R. Gliebe, T.F. Balsa, High velocity jet noise source locations and reduction, FAA-RD-76-79-II, 1978.
[16] G.K. Batchelor, *The Theory of Homogeneous Turbulence*, Cambridge University Press, Cambridge, 1960.
[17] J. Bridges, M.P. Wernet, Turbulence measurements of separate flow nozzles with mixing enhancement features, AIAA Paper 2002-2484, 2002.
[18] C.K.W. Tam, L. Auriault, Mean flow refraction effects on sound radiated from localized sources in a jet, *Journal of Fluid Mechanics* 370 (1998) 149–174.
[19] T.F. Balsa, The far-field of high frequency convected singularities in sheared flows, with an application to jet noise prediction, *Journal of Fluid Mechanics* 74 (1976) 193–208.
[20] W.T. Chu, Turbulence measurements relevant to jet noise, Institute for Aerospace Studies UTIAS Report No. 119, University of Toronto, Canada, 1966.
[21] A.A. Townsend, *The Structure of Turbulent Shear Flow*, Cambridge University Press, Cambridge, 1976.
[22] P.J. Morris, F. Farassat, Acoustic analogy and alternative theories for jet noise prediction, *American Institute of Aeronautics and Astronautics Journal* 40 (2002) 671–680.